


Article

# Characteristics of the *s*-Wave Symmetry Superconducting State in the BaGe<sub>3</sub> Compound

Kamila A. Szewczyk <sup>1,\*</sup> , Ewa A. Drzazga-Szcześniak <sup>2</sup>, Marcin W. Jarosik <sup>2</sup>,  
Klaudia M. Szcześniak <sup>3</sup> and Sandra M. Binek <sup>1</sup>

<sup>1</sup> Division of Theoretical Physics, Institute of Physics, Jan Długosz University in Częstochowa, Ave. Armii Krajowej 13/15, 42-200 Częstochowa, Poland

<sup>2</sup> Institute of Physics, Częstochowa University of Technology, Ave. Armii Krajowej 19, 42-200 Częstochowa, Poland

<sup>3</sup> Faculty of Chemistry, University of Warsaw, Pasteura 1, 02-093 Warsaw, Poland

\* Correspondence: kamila.szewczyk@ajd.czest.pl

Received: 29 June 2019; Accepted: 22 July 2019; Published: 1 August 2019



**Abstract:** Thermodynamic properties of the *s*-wave symmetry superconducting phase in three selected structures of the BaGe<sub>3</sub> compound (*P*<sub>63</sub>/*mmc*, *Amm*2, and *I*4/*mmm*) were discussed in the context of DFT results obtained for the Eliashberg function. This compound may enable the implementation of systems for quantum information processing. Calculations were carried out within the Eliashberg formalism due to the fact that the electron–phonon coupling constant falls within the range  $\lambda \in \langle 0.73, 0.86 \rangle$ . The value of the Coulomb pseudopotential was assumed to be 0.122, in accordance with the experimental results. The value of the Coulomb pseudopotential was assumed to be 0.122, in accordance with the experimental results. The existence of the superconducting state of three different critical temperature values, namely, 4.0 K, 4.5 K and 5.5 K, depending on the considered structure, was stated. We determined the differences in free energy ( $\Delta F$ ) and specific heat ( $\Delta C$ ) between the normal and the superconducting states, as well as the thermodynamic critical field ( $H_c$ ) as a function of temperature. A drop in the  $H_c$  value to zero at the temperature of 4.0 K was observed for the *P*<sub>63</sub>/*mmc* structure, which is in good accordance with the experimental data. Further, the values of the dimensionless thermodynamic parameters of the superconducting state were estimated as:  $R_\Delta = 2\Delta(0)/k_B T_c \in \{3.68, 3.8, 3.8\}$ ,  $R_C = \Delta C(T_c)/C^N(T_c) \in \{1.55, 1.71, 1.75\}$ , and  $R_H = T_c C^N(T_c)/H_c^2(0) \in \{0.168, 0.16, 0.158\}$ , which are slightly different from the predictions of the Bardeen–Cooper–Schrieffer theory ( $[R_\Delta]_{BCS} = 3.53$ ,  $[R_C]_{BCS} = 1.43$ , and  $[R_H]_{BCS} = 0.168$ ). This is caused by the occurrence of small retardation and strong coupling effects.

**Keywords:** *s*-wave symmetry Eliashberg formalism; BaGe<sub>3</sub> superconductor; thermodynamic properties

**PACS:** 74.20.Fg, 74.25.Bt, 74.62.Fj

## 1. Introduction

Ba–Ge type compounds are intensively studied with respect to the broad range of their possible technological applications, especially in thermoelectric devices [1,2], which are used for energy production and cooling. They are usually designed to acquire energy from the waste heat sources, e.g., from industrial or chemical processes [3]. It should be emphasized here that superconducting properties of the Ba–Ge type

compounds are used for the implementation of systems that perform quantum information processing [4]. Relevant information on the various forms of quantum correlations can be found in [5–8]. Particularly noteworthy is [9], in which the arrangement called the nonlinear quantum scissors was proposed for the first time. It allows calculations to be made on quantum states in a Hilbert space with a finite dimension.

Ba–Ge type compounds are well worth the attention with respect to their interesting low-temperature thermodynamic properties, including the *s*-wave symmetry superconducting ones [10,11]. It was pointed out, in particular, that the  $\text{Ba}_{24}\text{Ge}_{100}$  system undergoes a transition to the superconducting state at the temperature of 0.24 K [12–14], similarly as the  $\text{Ba}_{24}\text{Si}_{100}$  one. This discovery resulted in a great deal of research work concerning the physical properties of the  $\text{Ba}_{24}\text{Ge}_{100}$  material [15,16], which included studies on the interaction of rattling phonons [2]. It is believed that the highly efficient thermoelectric conversion realised by the unusually low thermal conductivity in these materials is closely related to phonons of such a type. Explanation of this concept, as well as its implementation in thermoelectric devices, is one of the most intriguing research problems in the recent twenty years [2,17]. It is worth noting that the superconducting state in the  $\text{Ba}_{24}\text{Ge}_{100}$  compound is also induced by the rattling phonons. Let us take note of the reader, the superconducting properties in functional materials, the structural parameters, the thermal conductivity, and the magnetic properties which are also examined. In this respect, special attention is given to functional oxides [18–20].

In another case, induction of the *s*-wave symmetry superconducting phase was experimentally observed in the  $\text{BaGe}_3$  compound of the  $P6_3/mmc$  crystalline structure at the temperature of 4 K [21]. The existence of the superconducting state was also stated in compounds of the  $\text{CaGe}_3$  and the  $\text{SiGe}_3$  types, for which the critical temperature value fell within the range from 4 K to 7.4 K. The performed *ab initio* calculations revealed that the materials, which we are going to consider here, belong to the family of *s*-wave symmetry superconductors with an electron–phonon pairing mechanism [22,23]. The superconductivity in the  $\text{BaGe}_3$  compound is induced by the relatively strong electron–phonon coupling (indicated by the relatively large value of  $\lambda$ ), which compensates for the low value of the logarithmic phonon frequency  $\omega_{\text{ln}}$  (see Table 1). The small value of  $\omega_{\text{ln}}$  results from the large atomic masses  $M$  of Ba and Ge atoms ( $\omega_{\text{ln}} \sim 1/\sqrt{M}$ ). The shape of the Eliashberg function  $\alpha^2F(\omega)$  and the integrated  $\lambda(\omega)$  for the *Amm*2 structure were presented in Reference [24]. Phonon modes from various areas contribute uniformly to the increase in  $\lambda$ , which implies the isotropic electron–phonon coupling. Additionally, the high value of the electron density of states at the Fermi level was confirmed, so that the formation of condensate of Cooper pairs is facilitated. Calculations were carried out by means of the VASP program employing the finite displacement method and by means of the ABINIT program using the linear response method. Using the DFT method, one can also model the stoichiometry of the samples (e.g., the functional [25]) in the context of their relationship with magnetic properties.

However, it should be borne in mind that the oxygen excess and deficit can increase and decrease the oxidation degree of cations. The changing of charge state of cations as the consequence of changing of oxygen content changes such magnetic parameters as total magnetic moment and Curie point, as well as such electrical parameters as activation energy and band gap. Moreover, oxygen vacancies affect exchange interactions. Intensity of exchange interactions decreases with oxygen vacancy concentration increasing. Exchange near the oxygen vacancies is negative according to the Goodenough–Kanamori empirical rules. Oxygen vacancies should lead to the formation of the frustration and weak magnetic state such as spin glass [26].

Pressure simulations were additionally performed for the  $\text{BaGe}_3$  compound. It was found that both the value of the electron–phonon coupling constant ( $\lambda$ ) and the value of critical temperature ( $T_c$ ) decrease with an increase in pressure [24,27]. Interestingly, there are two possible ways of  $\text{BaGe}_3$  crystallization under high pressure (not exceeding 15 GPa, however), resulting in two different structures, namely, *Amm*2 and *I4/mmm* [21,24], both remaining metastable even after lowering the pressure down to normal

conditions. Two newly discovered structures, *Amm2* and *I4/mmm*, exhibit some interesting properties. The superconducting state can be induced in both, at the critical temperature value equal to 4.5 K and 5.5 K, respectively. The *Amm2* phase is dynamically stable. It consists of clusters built of Ge atoms and triangular prisms formed by Ba atoms and intercalated with Ge atoms [24]. Such a structure has not been observed in any other compound of this group, which distinguishes the *Amm2* phase from the two others. The *I4/mmm* structure is very similar to the previously observed structure of the  $\text{CaGe}_3$  and the  $\text{XSi}_3$  compounds, where  $\text{X} = \text{Ca}$ ,  $\text{Y}$  or  $\text{Lu}$  [23]. The  $\text{Ge}_2$  dimers form square prisms in this crystalline structure. Theoretical predictions point out that the *I4/mmm* phase is dynamically stable under normal conditions.

The latest experimental research concerning the  $\text{BaGe}_3$  compound was carried out in 2016 [28]. The system was synthesized under high pressure and at high temperature ( $p = 15$  GPa,  $T = 1300$  K) and the generation of a new structure, classified as *tI32*, was observed. Metallic type electrical conductivity was stated, and the transition to the superconducting state occurred at the temperature of 6.5 K, which still remains the highest recorded critical temperature of this compound.

In the presented work, we are going to determine all the interesting thermodynamical properties of the *s*-wave symmetry superconducting state induced in the  $\text{BaGe}_3$  compound for three crystalline structures: *P6<sub>3</sub>/mmc*, *Amm2*, and *I4/mmm*.

**Table 1.** Selected values of the characteristic parameters of the *s*-wave symmetry superconducting state for the respective structures of the  $\text{BaGe}_3$  compound (results obtained using Eliashberg's formalism based on DFT data [24]). Thermodynamic parameters appearing in the table have been defined in the text of the work. Their meaning is carefully discussed in [29].

Structure	BaGe <sub>3</sub> Compound		
	<i>P6<sub>3</sub>/mmc</i>	<i>Amm2</i>	<i>I4/mmm</i>
$\lambda$	0.73	0.86	0.86
$\omega_{\text{ln}}(\text{meV})$	10.548	8.21	10.01
$T_c$ (K)	4.0	4.5	5.5
$r$	0.033	0.047	0.047
$R_\Delta$	3.68	3.8	3.8
$R_C$	1.55	1.71	1.75
$R_H$	0.168	0.16	0.158

## 2. Theoretical Model

The electron–phonon interaction in the  $\text{BaGe}_3$  compound is relatively strong, which is confirmed by the relatively high values of the electron–phonon coupling constant:  $\lambda = 0.73$  for the *P6<sub>3</sub>/mmc* structure and  $\lambda = 0.86$  for the two other structures, i.e. *Amm2* and *I4/mmm* ones [24] (see Table 1). Therefore we used the *s*-wave symmetry Eliashberg formalism, being a generalization of the BCS mean field theory [30,31], to determine the thermodynamic properties of the superconducting state in the considered systems. It should be remembered that the conventional BCS theory studies the results correctly only in the weak electron–phonon coupling limit ( $\lambda < 0.3$ ).

The *s*-wave symmetry Eliashberg equations on the imaginary axis were solved in the self-consistent way for the whole considered temperature range. In the mixed representation, however, we analysed them only for selected temperature values [29,32,33], for which the induction and the extinction of the superconducting state can be most easily observed.

The Eliashberg equations on the imaginary axis take the form of:

$$\varphi_n = \frac{\pi}{\beta} \sum_{m=-M}^M \frac{K(i\omega_n - i\omega_m) - \mu^* \theta(\omega_c - |\omega_m|)}{\sqrt{\omega_m^2 Z_m^2 + \varphi_m^2}} \varphi_m, \quad (1)$$

and

$$Z_n = 1 + \frac{1}{\omega_n} \frac{\pi}{\beta} \sum_{m=-M}^M \frac{K(i\omega_n - i\omega_m)}{\sqrt{\omega_m^2 Z_m^2 + \varphi_m^2}} \omega_m Z_m. \quad (2)$$

The *s*-wave symmetry order parameter is defined by the ratio:  $\Delta_n = \varphi_n / Z_n$ , where  $\varphi_n = \varphi(i\omega_n)$  represents the order parameter function and  $Z_n = Z(i\omega_n)$  is the wave function renormalization factor. Both functions depend directly on the fermionic Matsubara frequency  $\omega_n = \pi k_B T (2n - 1)$ , where  $k_B$  denotes the Boltzmann constant. The pairing kernel is given by the formula:  $K(z) = 2 \int_0^{+\infty} d\omega \frac{\omega}{\omega^2 - z^2} \alpha^2 F(\omega)$ , where  $\alpha^2 F(\omega)$  is the Eliashberg function. This function models the electron–phonon interaction. It should be noted that the numerical calculations related to the determination of the Eliashberg function were carried out for the ideal crystal structure. In the case of heterogeneity of the system (e.g., crystallites), one can expect the change in the thermodynamic properties of the superconducting phase, if the value of the electron and phonon density of states change. It is also important to change the matrix elements of the electron–phonon interaction. Analogous effects are also observed by examining the magnetic or electric properties of the crystals [34]. In the case of small impurities, Anderson’s theorem for the superconducting state with *s*-wave symmetry decides that the value of  $T_c$  will not change [35].

Note that the electron correlations do not contribute to the pairing potential. This means that the order parameter has only *s*-wave symmetry. The depairing electron correlations are modeled by the Coulomb pseudopotential ( $\mu^*$ ), which can be defined by the formula [36]:  $\mu^* = \mu / [1 + \mu \ln(\omega_e / \omega_{ph})]$ , where  $\mu = \rho(0) U$ , with an accuracy of the first order with respect to the the Coulomb potential ( $U$ ). The symbols  $\rho(0)$ ,  $\omega_e$ , and  $\omega_{ph}$  occurring in the formula denote the electronic density of states at the Fermi level, the characteristic electron frequency, and the characteristic phonon frequency, respectively. In our considerations we assumed the experimentally determined value of  $\mu^* = 0.122$ , which was found for the  $P6_3/mmc$  structure. The symbol  $\theta$  represents the Heaviside function. The value of the characteristic cutoff frequency in the Eliashberg theory should fall within the range  $\omega_c \in \langle 3\Omega_{\max}, 10\Omega_{\max} \rangle$ . We assumed  $\omega_c = 3\Omega_{\max}$  in our calculations. Note that the choice of  $\omega_c$  does not change the value of the thermodynamic functions that characterize the superconducting state. Only the value of the characteristic phonon frequency ( $\Omega_c$ ) is changed, which is the fitting parameter. The maximum phonon frequency is equal to  $\Omega_{\max} = 30$  meV for the three crystalline structures considered here.

The Eliashberg function and the Coulomb pseudopotential are two input parameters for the Eliashberg equations. In the considered system, the Eliashberg functions were substituted by the respective coupling constants:  $\lambda = 2 \int_0^{+\infty} d\omega \alpha^2 F(\omega) / \omega$ . There was also introduced the characteristic phonon frequency ( $\Omega_c$ ), which serves as the parameter fitting the model to the experimental data (to the value of the critical temperature).

The Eliashberg equations were solved numerically. We made use of the finite difference approximation of Newton’s method and assumed  $M = 1100$ , like in our other studies [37–40]. We obtained the stability of solutions of the Eliashberg equations within the temperature range from  $T_0 = 0.6$  K to  $T_c$ .

The Eliashberg equations defined on the imaginary axis allow to determine most of the thermodynamic properties of the superconducting phase, nevertheless, they do not give full information. For the purpose of finding the physical value of the order parameter, the Eliashberg equations should be solved in the mixed representation ( $\varphi_n \rightarrow \varphi(\omega)$  and  $Z_n \rightarrow Z(\omega)$ ). The *s*-wave symmetry Eliashberg

equations in mixed representation can be obtained by the analytic continuation method [33]. They take the form:

$$\begin{aligned} \varphi(\omega + i\delta) = & \pi k_B T \sum_{m=-M}^M [K(\omega - i\omega_m) - \mu^* \theta(\omega_c - |\omega_m|)] \frac{\varphi_m}{\sqrt{\omega_m^2 Z_m^2 + \varphi_m^2}} \\ & + i\pi \int_0^{+\infty} d\omega' \alpha^2 F(\omega') \left[ f_{BE}(\omega') + f_{FD}(\omega' - \omega) \right] \times \frac{\varphi(\omega - \omega' + i\delta)}{\sqrt{(\omega - \omega')^2 Z^2(\omega - \omega' + i\delta) - \varphi^2(\omega - \omega' + i\delta)}} \\ & + i\pi \int_0^{+\infty} d\omega' \alpha^2 F(\omega') \left[ f_{BE}(\omega') + f_{FD}(\omega' + \omega) \right] \times \frac{\varphi(\omega + \omega' + i\delta)}{\sqrt{(\omega + \omega')^2 Z^2(\omega + \omega' + i\delta) - \varphi^2(\omega + \omega' + i\delta)}}, \end{aligned} \quad (3)$$

and

$$\begin{aligned} Z(\omega + i\delta) = & 1 + \frac{i}{\omega} \pi k_B T \sum_{m=-M}^M K(\omega - i\omega_m) \frac{\omega_m Z_m}{\sqrt{\omega_m^2 Z_m^2 + \varphi_m^2}} \\ & + \frac{i\pi}{\omega} \int_0^{+\infty} d\omega' \alpha^2 F(\omega') \left[ f_{BE}(\omega') + f_{FD}(\omega' - \omega) \right] \times \frac{(\omega - \omega') Z(\omega - \omega' + i\delta)}{\sqrt{(\omega - \omega')^2 Z^2(\omega - \omega' + i\delta) - \varphi^2(\omega - \omega' + i\delta)}} \\ & + \frac{i\pi}{\omega} \int_0^{+\infty} d\omega' \alpha^2 F(\omega') \left[ f_{BE}(\omega') + f_{FD}(\omega' + \omega) \right] \times \frac{(\omega + \omega') Z(\omega + \omega' + i\delta)}{\sqrt{(\omega + \omega')^2 Z^2(\omega + \omega' + i\delta) - \varphi^2(\omega + \omega' + i\delta)}}, \end{aligned} \quad (4)$$

where the symbols  $f_{BE}(\omega)$  and  $f_{FD}(\omega)$  stand for the Bose–Einstein and the Fermi–Dirac functions, respectively.

### 3. Numerical Results

We began the analysis of properties of the superconducting state from the determination of the characteristic phonon frequency  $\Omega_c$  from the equation:  $[\Delta_{n=1}(\Omega_c)]_{T=T_c} = 0$ . We obtained the following values: 8.5 meV, 6.7 meV, and 8.3 meV, for the  $P6_3/mmc$ , the  $Amm2$ , and the  $I4/mmm$  structure, respectively. Full numerical results are presented in Figure 1.

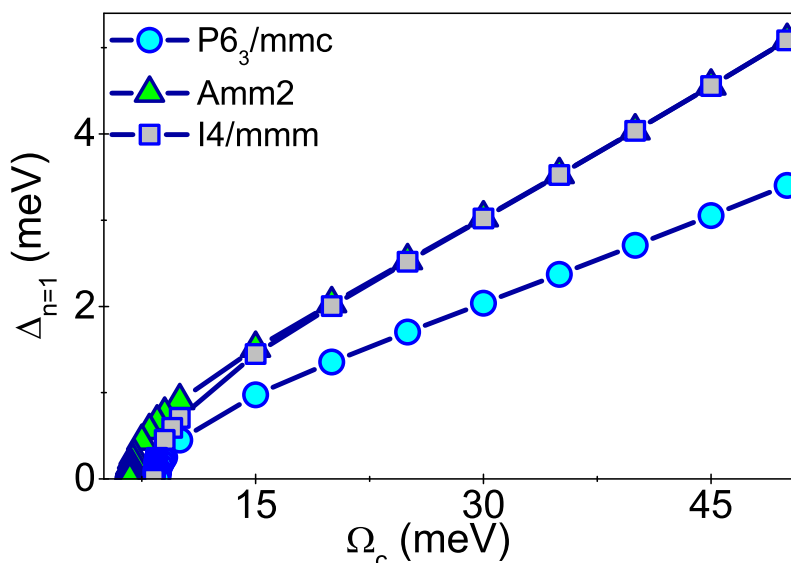


**Figure 1.** The dependence of the  $s$ -wave symmetry order parameter on the characteristic phonon frequency ( $T = T_c$ ).

Then, we solved the  $s$ -wave symmetry Eliashberg equations on the imaginary axis. We were interested in the dependence of the order parameter ( $\Delta_{n=1}(T)$ ) and the wave function renormalisation

factor ( $Z_{n=1}(T)$ ) on temperature (Figure 2). As it is well known, the order parameter takes zero value for  $T \geq T_c$ , what allows to estimate the critical temperature. Its respective values were found to be:  $T_c = 4.0$  K for  $P6_3/mmc$ ,  $T_c = 4.5$  K for  $Amm2$ , and  $T_c = 5.5$  K for  $I4/mmm$  structure (see the upper plot in Figure 2). Note that the obtained  $\Delta_{n=1}(T)$  functions can be compared with experimental data. As a result, it will be possible to identify the crystal structure of the tested system.

Please note that the results obtained by means of Eliashberg equations can be parameterised in the following way:

$$\Delta_{n=1}(T) = \Delta_{n=1}(0) \sqrt{1 - (T/T_c)^\gamma}, \quad (5)$$

where  $\gamma = 3.3$  for  $P6_3/mmc$  and  $\gamma = 3.35$  for both other structures. It is worth mentioning here that the parameter  $\gamma$  is equal to 3.0 in the standard BCS theory [41]. Additionally,  $\Delta_{n=1}(0) \in \{0.63, 0.73, 0.89\}$  meV for  $P6_3/mmc$ ,  $Amm2$  and  $I4/mmm$  structures, respectively.

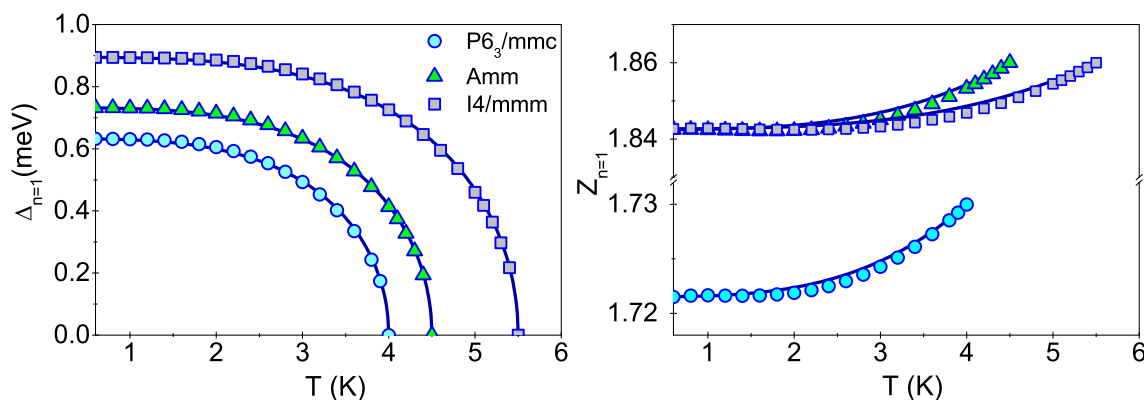


**Figure 2.** The dependence of the  $s$ -wave symmetry order parameter on the temperature (upper plot). The wave function renormalization factor versus temperature (lower plot). Numerical results obtained within the Eliashberg formalism are marked by the point symbols, whereas the solutions obtained on the basis of Equations (5) and (6) are plotted as dark blue solid lines.

The lower plot in Figure 2 presents the wave function renormalization factor, the value of which slightly increases with an increase in temperature and reaches its maximum at  $T_c$ . This maximum value should be comparable with the one obtained from the formula:  $Z_{n=1}(T_c) = \lambda + 1$ . The latter, after obvious calculations, gives the following maximum values for the considered case:  $Z_{n=1}(T_c) = 1.73$  for the  $P6_3/mmc$  structure and  $Z_{n=1}(T_c) = 1.86$  for both other structures under consideration. One can easily see that the maximum values achieved from the numerical solution within the Eliashberg formalism are in good agreement with the ones calculated from the mentioned formula (see Figure 2). Additionally, the full profile of the wave function renormalization factor can be approximately reproduced with the formula:

$$Z_{n=1}(T) = Z_{n=1}(0) + [Z_{n=1}(T_c) - Z_{n=1}(0)] \left( \frac{T}{T_c} \right)^\gamma, \quad (6)$$

where  $Z_{n=1}(0) = 1.72$  for  $P6_3/mmc$  and  $Z_{n=1}(0) = 1.84$  for both other structures. Figure 2 indicates the results achieved numerically from the Eliashberg equations by point symbols (triangles, squares, or disks), while the fitting functions are shown as dark blue solid lines.

Subsequently, we determined the temperature dependence of the difference in free energy between the superconducting and the normal state. We used the following formula normalized with respect to the electronic density of states at the Fermi level [42]:

$$\frac{\Delta F}{\rho(0)} = -2\pi k_B T \sum_{n=1}^M \left[ \sqrt{\omega_n^2 + (\Delta_n)^2} - |\omega_n| \right] \times \left[ Z_n^{(S)} - Z_n^{(N)} \frac{|\omega_n|}{\sqrt{\omega_n^2 + (\Delta_n)^2}} \right]. \quad (7)$$

Symbols  $Z_n^{(S)}$  and  $Z_n^{(N)}$  in the above formula represent the wave function renormalization factor for the superconducting (S) and the normal (N) states, respectively.

The negative values of the difference in free energy over the whole temperature range ( $T_0 \leq T \leq T_c$ ), shown in Figure 3 (lower section), confirm the thermodynamic stability of the superconducting state in the crystalline structures under consideration.

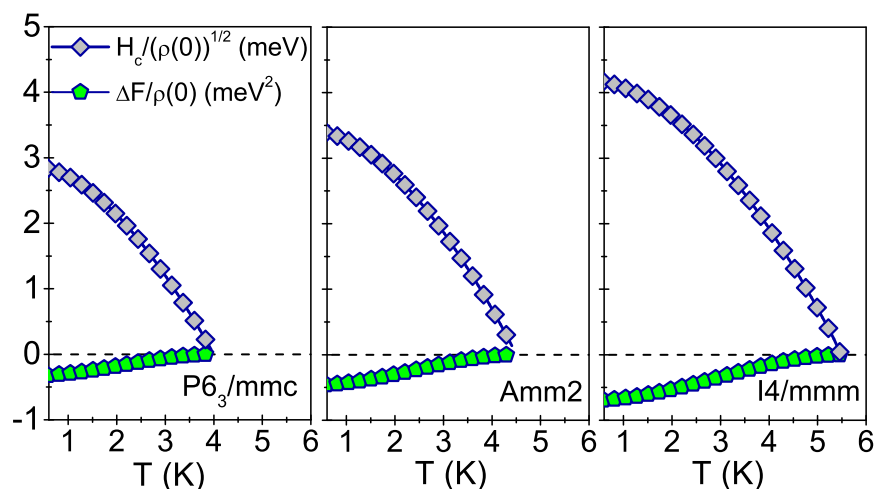


**Figure 3.** Thermodynamic critical field (upper section) and the difference in free energy between the superconducting and the normal state (lower section) versus temperature.

The acquired knowledge of the temperature dependence of the difference in free energy allowed us to estimate further significant thermodynamic properties of the investigated compound. Our first step was the calculation of the thermodynamic critical field by means of the formula:

$$\frac{H_c}{\sqrt{\rho(0)}} = \sqrt{-8\pi \frac{\Delta F}{\rho(0)}}. \quad (8)$$

Its profile plotted against temperature is shown in Figure 3 (upper section). One can conclude from it that the value of the thermodynamic critical field decreases as the temperature increases, and eventually drops down to zero at  $T_c$ . The results presented in Figure 3 are in accordance with the experiment carried out for the P6<sub>3</sub>/mmc structure, during which the Meissner effect was observed at the temperature  $T = 4.0$  K [21].



Subsequently, the difference in the specific heat ( $\Delta C = C^S - C^N$ ) between the superconducting(S) and the normal (N) state was determined. To do this, we used the formula:

$$\frac{\Delta C(T)}{k_B \rho(0)} = -\frac{1}{\beta} \frac{d^2 [\Delta F / \rho(0)]}{d(k_B T)^2}. \quad (9)$$

The specific heat for the normal state can be determined by means of the formula:  $C^N / k_B \rho(0) = \gamma / \beta$ , where  $\gamma = \frac{2}{3} \pi^2 (1 + \lambda)$  is the Sommerfeld constant. Numerical results are presented in Figure 4 and indicate linear growth. On the other hand, it can be seen that the specific heat in the superconducting state increases exponentially as the temperature rises. Then, a rapid jump is observed at the critical temperature, followed by further changes proceeding in a way characteristic of the metallic phase. It should be clearly emphasized that the obtained specific heat curves, as well as the thermodynamic critical field curves, can be directly compared with data obtained experimentally.

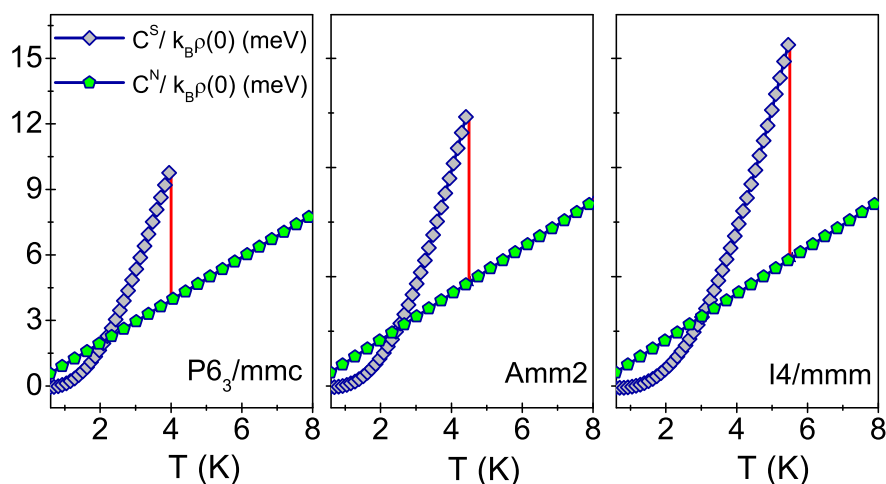


**Figure 4.** The specific heat for the superconducting state ( $C^S$ ) and the normal state ( $C^N$ ) versus temperature. The vertical red lines denote the characteristic jump of the specific heat at  $T_c$ .

The successive stage of calculations consisted in solving the  $s$ -wave symmetry Eliashberg equations in mixed representation. In this way, we obtained functions describing both the order parameter and the wave function renormalization factor on the real axis, so that we could analyse the damping effect. The physical value of the order parameter can be obtained by means of the formula:  $\Delta(T) = \text{Re}[\Delta(\omega = \Delta(T), T)]$ . The results are shown in Figure 5. Each row of charts corresponds to one of the examined structures. The frequency range was assumed to extend from 0 to 50 meV. Such an interval was selected with respect to the construction of the Eliashberg function given for the *Amm2* structure [24], which takes the non-zero values near (2.25) meV. However, the frequency range for the other structures is remarkably greater, even reaching 45 meV, as can be seen in the charts (Figure 5). The presented plots clearly show that only the real part of the order parameter takes the non-zero values for low frequencies (up to 8 meV). This is evidence of the existence of Cooper pairs with a long lifetime. For higher frequencies, also the imaginary part of the order parameter takes non-zero values. This indicates the existence of Cooper pairs with a finite lifetime. The rapid increase of the damping effects can be seen, especially in the frequency range from about 8 meV to about 30 meV. It is caused by the rather strong electron–phonon coupling within this range.



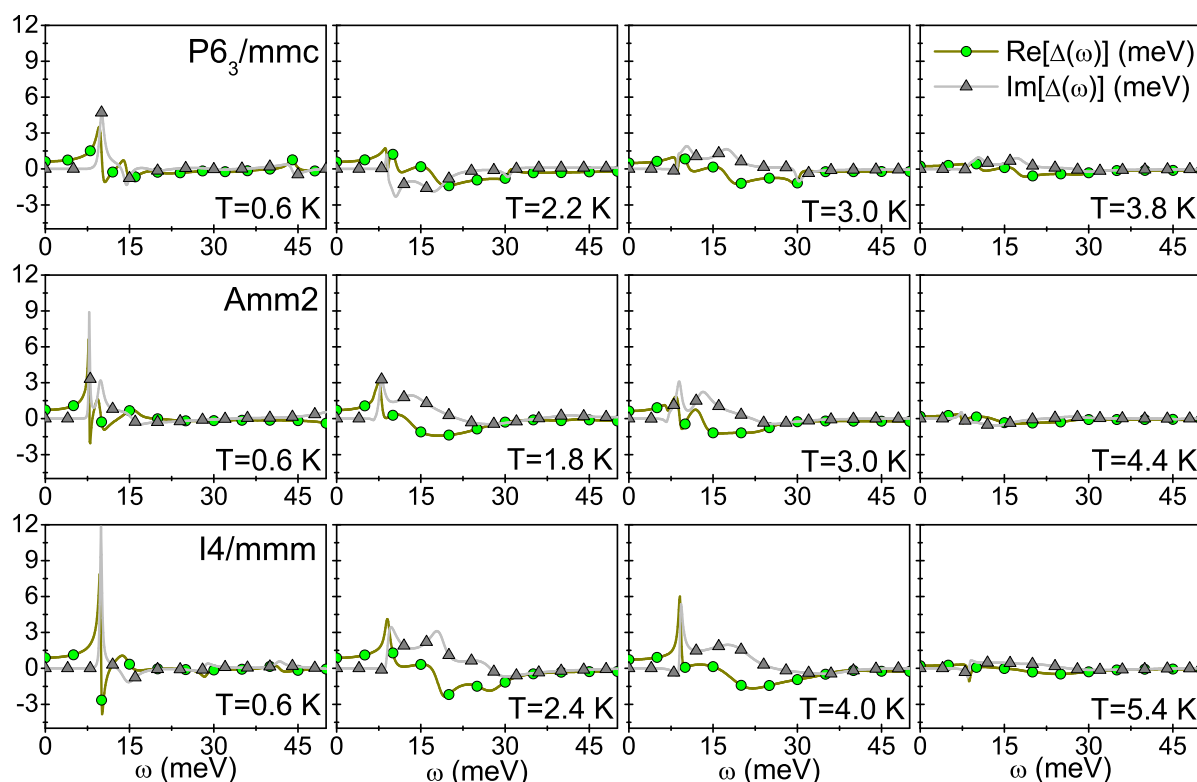


**Figure 5.** The real and the imaginary part of the  $s$ -wave symmetry order parameter for selected temperature values. The first row of charts presents results for the  $P6_3/mmc$  structure, the second for  $Amm2$ , and the third for  $I4/mmm$ .

The numerical values obtained for the order parameter on the real axis  $\text{Re}[\Delta(\omega)]$  (Figure 5) are in accordance with the values on the imaginary axis  $\Delta_{n=1}$  (Figure 2), what confirms the correctness of the performed calculations.

During the last step, we determined the dimensionless thermodynamic parameters of the superconducting state:  $R_\Delta = 2\Delta(0)/k_B T_c$ ,  $R_C = \Delta C(T_c)/C^N(T_c)$ , and  $R_H = T_c C^N(T_c)/H_c^2(0)$ . One can notice that the results presented in Table 1 for the  $P6_3/mmc$  structure are quite close to the predictions of the BCS theory ( $[R_\Delta]_{BCS} = 3.53$ ,  $[R_C]_{BCS} = 1.43$ , and  $[R_H]_{BCS} = 0.168$  [30,31]). Greater divergences can be seen for the two other structures. The apparently different results are directly related to the presence of both the retardation and the strong-coupling effects, which in turn are characterised by the ratio  $r = k_B T_c/\omega_{ln}$ . This ratio takes the following values:  $r = 0.03$  for the  $P6_3/mmc$  structure, and  $r = 0.05$  for the two other structures (exact values are given in Table 1). The lack of the above mentioned effects in the BCS theory could be expressed as  $r \rightarrow 0$ .

#### 4. Summary

Slack's predictions about clathrates containing additional atoms as the promising thermoelectric materials [43] encouraged many researchers to seek more such systems. One of them is the  $\text{BaGe}_3$  compound, for which the induction of the  $s$ -wave symmetry superconducting state at the critical temperature of 4.0 K in the  $P3_6/mmc$  crystalline structure was observed during experiments [21]. Moreover, two other structures of this compound were discovered on account of investigations, namely,  $Amm2$  and  $I4/mmm$  [24], synthesized under high pressure and remaining thermodynamically stable under normal conditions, which undergo the  $s$ -wave symmetry superconductor–metal phase transition at

the temperature of 4.5 K and 5.5 K, respectively. We determined the thermodynamic properties of the superconducting state for the reported structures using the formalism of the *s*-wave Eliashberg equations by reason of the occurrence of high values of the electron–phonon coupling constants ( $\lambda^{P3_6/mmc} = 0.73$ ,  $\lambda^{Amm2} = \lambda^{I4/mmm} = 0.86$ ). In our calculations, we assumed that  $\mu^* = 0.122$ , in consistency with the experimental results [21,24]. We determined the thermodynamic functions of the superconducting state which allowed us to find the nondimensional parameters  $R_\Delta$ ,  $R_C$ , and  $R_H$ . As far as the BCS theory is considered, these parameters are universal constants and their values are as follows:  $[R_\Delta]_{BCS} = 3.53$ ,  $[R_C]_{BCS} = 1.43$ , and  $[R_H]_{BCS} = 0.168$  [30,31]. Within the Eliashberg formalism, we achieved the following results:  $R_\Delta = 3.68$ ,  $R_C = 1.55$ , and  $R_H = 0.168$  for the  $P3_6/mmc$  structure;  $R_\Delta = 3.8$ ,  $R_C = 1.71$ , and  $R_H = 0.16$  for the  $Amm2$  structure; and finally  $R_\Delta = 3.8$ ,  $R_C = 1.75$ , and  $R_H = 0.158$  for the  $I4/mmm$  structure. Our results differ slightly from the predictions of the BCS theory because of the presence of small retardation and strong-coupling effects (the relevant parameter  $r = k_B T_c / \omega_{ln}$  is less than  $\sim 0.05$  for all crystalline structures of the  $BaGe_3$  compound).

It should be noted that, in the case of  $BaGe_3$ , the Eliashberg formalism we used describes the properties of the superconducting state at the quantitative level. This means that the thermodynamic functions are determined very precisely. Due to the relatively low value of the Coulomb pseudopotential, there is no need for any modification of the presented theory.

**Author Contributions:** Conceptualization, E.A.D.-S.; methodology, M.W.J.; software, E.A.D.-S. and M.W.J.; validation, K.A.S., M.W.J. and E.A.D.-S.; formal analysis, K.A.S.; investigation, K.A.S., K.M.S. and S.M.B.; resources, E.A.D.-S. and M.W.J.; data curation, K.A.S.; visualization, K.M.S. and S.M.B.; supervision, E.A.D.-S.; project administration, E.A.D.-S. and M.W.J.; funding acquisition, K.A.S.

**Funding:** The results described in the present work were achieved with financial support of a Grant for Young Scientist (grant number DSM/WMP/6548/2018) provided by the Jan Długość University in Częstochowa.

**Conflicts of Interest:** The authors declare no conflict of interest. The funders had no role in the design of the study; in the collection, analyses, or interpretation of data; in the writing of the manuscript, or in the decision to publish the results.

## References

- Kim, S.J.; Hu, S.; Uher, C.; Hogan, T.; Huang, B.; Corbett, J.D.; Kanatzidis, M.G. Structure and Thermoelectric Properties of  $Ba_6Ge_{25-x}$ ,  $Ba_6Ge_{23}Sn_2$ , and  $Ba_6Ge_{22}In_3$ : Zintl Phases with a Chiral Clathrate Structure. *J. Solid State Chem.* **2000**, *153*, 321–329.
- Paschen, S.; Tran, V.H.; Baenitz, M.; Carrillo-Cabrera, W.; Grin, Y.; Steglich, F. Clathrate  $Ba_6Ge_{25}$ : Thermodynamic, magnetic, and transport properties. *Phys. Rev. B* **2002**, *65*, 134435.
- Martin, P. Thermoelectric Materials and Applications. *News Bull.* **2005**, *2005*, 30.
- Gu, X.; Kockum, A.F.; Miranowicz, A.; Liu, Y.X.; Nori, F. Microwave photonics with superconducting quantum circuits. *Phys. Rep.* **2017**, *1*, 718–719.
- Kalaga, J.K.; Kowalewska-Kudłaszyk, A.; Leoński, W.; Barasiński, A. Quantum correlations and entanglement in a model comprised of a short chain of nonlinear oscillators. *Phys. Rev. A* **2016**, *94*, 032304.
- Kalaga, J.K.; Leoński, W.; Szczęśniak, R. Quantum steering and entanglement in three-mode triangle Bose–Hubbard system. *Quantum Inf. Process.* **2017**, *16*, 265.
- Kalaga, J.K.; Leoński, W.; Peřina, J., Jr. Einstein–Podolsky–Rosen steering and coherence in the family of entangled three-qubit states. *Phys. Rev. A* **2018**, *97*, 042110.
- Kalaga, J.K.; Leoński, W. Quantum steering borders in three-qubit systems. *Quantum Inf. Process.* **2017**, *16*, 175.
- Leoński, W.; Tanaś, R. Possibility of producing the one-photon state in a kicked cavity with a nonlinear Kerr medium. *Phys. Rev. A* **1994**, *49*, R20.

10. Vaughey, J.T.; Miller, G.J.; Gravelle, S.; Leon-Escamilla, E.A.; Corbett, J.D. Synthesis, Structure, and Properties of  $BaGe_2$ : A Study of Tetrahedral Cluster Packing and Other Three-Connected Nets in Zintl Phases. *J. Solid State Chem.* **1997**, *133*, 501–507.
11. Evers, J.; Oehlinger, G.; Ott, H.R. Superconductivity of  $SrSi_2$  and  $BaGe_2$  with the  $\alpha - ThSi_2$ -type structure. *J. Less-Common Met.* **1980**, *69*, 389–391.
12. Fukuoka, H.; Ueno, K.; Yamanaka, S. High-pressure synthesis and structure of a new silicon clathrate  $Ba_{24}Si_{100}$ . *J. Organomet. Chem.* **2000**, *611*, 543–546.
13. Grosche, F.M.; Yuan, H.Q.; Carrillo-Cabrera, W.; Paschen, S.; Langhammer, C.; Kromer, F.; Sparn, G.; Baenitz, M.; Grin, Y.; Steglich, F. Superconductivity in the Filled Cage Compounds  $Ba_6Ge_{25}$  and  $Ba_4Na_2Ge_{25}$ . *Phys. Rev. Lett.* **2001**, *87*, 247003.
14. Yuan, H.Q.; Grosche, F.M.; Carrillo-Cabrera, W.; Pacheco, V.; Sparn, G.; Baenitz, M.; Schwarz, U.; Grin, Y.; Steglich, F. Interplay of superconductivity and structural phase transition in the clathrate  $Ba_6Ge_{25}$ . *Phys. Rev. Lett.* **2004**, *70*, 174512.
15. Kanetake, F.; Harada, A.; Mukuda, H.; Kitaoka, Y.; Rachi, T.; Tanigaki, K.; Itoh, K.M.; Haller, E.E.  $^{73}Ge$ - and  $^{135/137}Ba$ -NMR Studies of Clathrate Superconductor  $Ba_{24}Ge_{100}$ . *J. Phys. Soc. Jpn.* **2009**, *78*, 104710.
16. Tang, J.; Xu, J.; Heguri, S.; Fukuoka, H.; Yamanaka, S.; Akai, K.; Tanigaki, K. Electron-Phonon Interactions of  $Si_{100}$  and  $Ge_{100}$  Superconductors with  $Ba$  Atoms Inside. *Phys. Rev. Lett.* **2010**, *105*, 176402.
17. Shimono, Y.; Shibauchi, T.; Kasahara, Y.; Kato, T.; Hashimoto, K.; Matsuda, Y.; Yamaura, J.; Nagao, Y.; Hiroi, Z. Effects of Rattling Phonons on the Dynamics of Quasiparticle Excitation in the  $\beta$ -Pyrochlore  $KOs_2O_6$  Superconductor. *Phys. Rev. Lett.* **2007**, *98*, 257004.
18. Trukhanov, A.V.; Kostishyn, V.G.; Panina, L.V.; Korovushkin, V.V.; Turchenko, V.A.; Thakur, P.; Thakur, A.; Yang, Y.; Vinnik, D.A.; Yakovenko, E.S.; et al. Control of electromagnetic properties in substituted M-type hexagonal ferrites. *J. Alloys Compd.* **2018**, *754*, 247–256.
19. Trukhanov, A.V.; Trukhanov, S.V.; Kostishyn, V.G.; Panina, L.V.; Korovushkin, V.V.; Turchenko, V.A.; Vinnik, D.A.; Yakovenko, E.S.; Zagorodnii, V.V.; Launetz, V.L.; et al. Correlation of the atomic structure, magnetic properties and microwave characteristics in substituted hexagonal ferrites. *J. Magn. Magn. Mater.* **2018**, *462*, 127–135.
20. Trukhanov, A.V.; Kozlovskiy, A.L.; Ryskulov, A.E.; Uglov, V.V.; Kislitsin, S.B.; Zdorovets, M.V.; Trukhanov, S.V.; Zubar, T.I.; Astapovich, K.A.; et al. Control of structural parameters and thermal conductivity of BeO ceramics using heavy ion irradiation and post-radiation annealing. *Ceram. Int.* **2019**, *45*, 15412–15416.
21. Fukuoka, H.; Tomomitsu, Y.; Inumaru, K. High-Pressure Synthesis and Superconductivity of a New Binary Barium Germanide  $BaGe_3$ . *Inorg. Chem.* **2009**, *50*, 6372–6377.
22. Schnelle, W.; Ormeci, A.; Wosylus, A.; Meier, K.; Grin, Y.; Schwarz, U. Dumbbells of Five-Connected  $Ge$  Atoms and Superconductivity in  $CaGe_3$ . *Inorg. Chem.* **2012**, *51*, 5509–5511.
23. Schwarz, U.; Wosylus, A.; Rosner, H.; Schnelle, W.; Ormeci, A.; Meier, K.; Baranov, A.; Nicklas, M.; Leipe, S.; Müller, C.J.; et al. Dumbbells of Five-Connected Silicon Atoms and Superconductivity in the Binary Silicides  $MSi_3$  ( $M = Ca, Y, Lu$ ). *J. Am. Chem. Soc.* **2012**, *134*, 13558–13561.
24. Zurek, E.; Yao, Y. Theoretical Predictions of Novel Superconducting Phases of  $BaGe_3$  Stable at Atmospheric and High Pressures. *Inorg. Chem.* **2015**, *54*, 2875.
25. Trukhanov, S.V.; Trukhanov, A.V.; Vasiliev, A.N.; Szymczak, H. Frustrated Exchange Interactions Formation at Low Temperatures and High Hydrostatic Pressures in  $La_{0.70}Sr_{0.30}MnO_{2.85}$ . *J. Exp. Theor. Phys.* **2019**, *111*, 209.
26. Trukhanov, S.V.; Trukhanov, A.V.; Botez, C.E.; Adair, A.H.; Szymczak, H.; Szymczak, R. Magnetic State of the Structural Separated Anion Deficient  $La_{0.70}Sr_{0.30}MnO_{2.85}$  Manganite. *J. Exp. Theor. Phys.* **2019**, *113*, 819.
27. Chen, X.J.; Zhang, C.; Meng, Y.; Zhang, R.Q.; Lin, H.Q.; Struzhkin, V.V.; Mao, H.  $\beta - tin \rightarrow Imma \rightarrow sh$  Phase Transitions of Germanium. *Phys. Rev. Lett.* **2011**, *106*, 135502.
28. Castillo, R.; Baranov, A.I.; Burkhardt, U.; Cardoso-Gil, R.; Schnelle, W.; Bobnar, M.; Schwarz, U. Germanium Dumbbells in a New Superconducting Modification of  $BaGe_3$ . *Inorg. Chem.* **2016**, *55*, 4498.
29. Carbotte, J.P. Properties of boson-exchange superconductors. *Rev. Mod. Phys.* **1990**, *62*, 1027.
30. Bardeen, J.; Cooper, L.N.; Schrieffer, J.R. Microscopic theory of superconductivity. *Phys. Rev.* **1957**, *106*, 162.
31. Bardeen, J.; Cooper, L.N.; Schrieffer, J.R. Theory of superconductivity. *Phys. Rev.* **1957**, *108*, 1175.

32. Eliashberg, G.M. Interactions between electrons and lattice vibrations in a superconductor. *Sov. Phys. JETP* **1960**, *11*, 696.
33. Marsiglio, F.; Schossmann, M.; Carbotte, J.P. Iterative analytic continuation of the electron self-energy to the real axis. *Phys. Rev. B* **1988**, *37*, 4965.
34. Trukhanov, S.V.; Trukhanov, A.V.; Botez, C.E.; Adair, A.H.; Szymczak, H.; Szymczak, R. Phase separation and size effects in  $Pr_{0.70}Ba_{0.30}MnO_{3+\delta}$  perovskite manganites. *J. Phys. Condens. Matter* **2007**, *19*, 266214.
35. Anderson, P.W. Knight Shift in Superconductors. *Phys. Rev. Lett.* **1959**, *3*, 325.
36. Morel, P.; Anderson, P.W. Calculation of the superconducting state parameters with retarded electron-phonon interaction. *Phys. Rev.* **1962**, *125*, 1263.
37. Durajski, A.P.; Szczęśniak, R.; Li, Y. Non-BCS thermodynamic properties of  $H_2S$  superconductor. *Phys. C Supercond. Its Appl.* **2015**, *515*, 1–6.
38. Szczęśniak, D.; Szczęśniak, R. Thermodynamics of the hydrogen dominant potassium hydride superconductor at high pressure. *Solid State Commun.* **2015**, *212*, 1.
39. Duda, A.M.; Szewczyk, K.A.; Jarosik, M.W.; Szczęśniak, K.M.; Sowińska, M.A.; Szczęśniak, D. Characterization of the superconducting state in hafnium hydride under high pressure. *Phys. B Condens. Matter* **2018**, *536*, 275.
40. Szczęśniak, D.; Kaczmarek, A.Z.; Szczęśniak, R.; Turchuk, S.V.; Zhao, H.; Drzazga, E.A. Superconducting properties of under- and over-doped  $Ba_xK_{1-x}BiO_3$  perovskite oxide. *Mod. Phys. Lett. B* **2018**, *32*, 1850174.
41. Eschrig, H. *Theory of Superconductivity: A Primer*; Citeseer: State College, PA, USA, 2001.
42. Bardeen, J.; Stephen, M. Free-energy difference between normal and superconducting states. *Phys. Rev.* **1964**, *136*, A1485.
43. Slack, G.A. *CRC Handbook of Thermoelectrics*; Character 34; Rowe, D.M., Ed.; Chemical Rubber: Boca Raton, FL, USA, 1995.



© 2019 by the authors. Licensee MDPI, Basel, Switzerland. This article is an open access article distributed under the terms and conditions of the Creative Commons Attribution (CC BY) license (<http://creativecommons.org/licenses/by/4.0/>).